# Stable-unstable switching dynamics in semiconductor lasers with external cavities

Jia-Xin Dong,[1] Jingya Ruan,[1] Luan Zhang,[1] Jun-Ping Zhuang,[1] and Sze-Chun Chan[1,2,*]

[1]*Department of Electrical Engineering, City University of Hong Kong, Hong Kong, China*

[2]*State Key Laboratory of Terahertz and Millimeter Waves, City University of Hong Kong, Hong Kong, China*

(Received 13 December 2020; accepted 13 May 2021; published 28 May 2021)

Optical feedback in a semiconductor laser was recently used for photonic microwave square-wave generation by invoking quasiperiodicity for repeated switching between a stable stage of constant intensity and an unstable stage of intensity oscillations. Based on the Lang-Kobayashi model for a laser with external-cavity feedback, we investigate such stable-unstable switching dynamics. First, the model is verified to produce the stable-unstable switching dynamics as the feedback strength and delay are adjusted. The model agrees with former experiments in spite of previous doubts. Then, the analytical Hopf boundary for the minimum linewidth mode is derived to be matching the boundaries of the switching regions. Moreover, the trajectory in the plane of instantaneous frequency and gain is analyzed during the stable stage, where the laser is found to follow an ellipse in visiting different external cavity modes. Most importantly, an analytical derivation yields the switching period $\tau + \tau_\varepsilon$ that is slightly expanded from the feedback delay time $\tau$, where the expansion time $\tau_\varepsilon$ is found to be inversely proportional to the feedback strength. Such a switching period expansion explains the generation of a shifted frequency component below $1/\tau$ in quasiperiodic laser dynamics. The results generally contribute to understanding the switching dynamics in photonic microwave generation.

DOI: 10.1103/PhysRevA.103.053524

## I. INTRODUCTION

Semiconductor lasers under perturbations exhibit versatile nonlinear dynamics in a number of microwave and millimeter-wave photonic applications [1–4]. Applications in recent years include tunable millimeter-wave generation [5–7], phase noise reduction [8–10], square-wave generation [11–13], broadband random signal generation [14–17], high-speed reservoir computing [18–20], secure communications [21,22], and ranging [23–26]. As a form of perturbation, optical feedback has attracted continuous attention because of the simplicity in construction using an external cavity, which enabled the observations of some fundamental behaviors of a laser [27–34]. Recently developed direct measurements on the diode junction voltage and the optical frequency have further revealed the details of the dynamics [5,35,36].

For a single-mode laser subject to feedback, the dynamics is closely related to the relaxation resonance frequency and the frequencies of the external cavity modes (ECMs), which are roughly separated by the reciprocal of the feedback delay time $\tau$ [37,38]. These frequencies are usually incommensurate, resulting in the quasiperiodic route-to-chaos that comprises the following states [11,32]: A self-locking state yields a stable intensity as locked to an ECM [32,39]. A periodic state yields an unstable intensity that rapidly oscillates as the relaxation resonance is undamped [10,40]. A quasiperiodic state yields an oscillatory intensity with an undulating envelope when incommensurate frequency components are mixed [5,11]. A chaotic state appears when additional frequency components emerge [41,42]. Additionally, when biased near the threshold, the laser can hop around different ECMs for low-frequency fluctuations [35,43]. The laser with a short external cavity can emit intermittent chaos or regular pulse packages [44–46].

Recently, experiments in the long-cavity regime unveiled an interesting dynamics that switches periodically between a stable stage of constant intensity and an unstable stage of rapidly oscillatory intensity near the relaxation resonance [11,13]. The intensity oscillation switches off and on repeatedly at a switching period that is slightly longer than $\tau$. The stable-unstable switching dynamics can be understood as a form of quasiperiodicity involving the emergence of the incommensurate frequencies [10,36]. Such a dynamics was used to generate a microwave signal near the relaxation resonance frequency with square-wave modulation [13,47]. The signal can be obtained optically using a photodetector or electrically from the voltage across the laser [5,10]. It can be of low phase noise due to the external cavities for photonic microwave generation [48].

The Lang-Kobayashi model is considered because of its success in explaining a wide range of phenomena for semiconductor lasers under feedback [27,32]. The model was thoroughly analyzed in the plane of delayed optical phase difference and charge-carrier density [28,49]. Saddle-node bifurcations create ECMs including the maximum gain mode (MGM) and the minimum linewidth mode (MLM) [11,36]. Hopf bifurcations destabilize some ECMs in yielding oscillations near the relaxation resonance [29,32]. The model yielded explanations of phase noise reduction in self-locking states [49,50], quantification of the feedback conditions for different dynamical states [32,51], and a qualitative description of trajectories for intermittent chaos, low-frequency

*scchan@cityu.edu.hk

 

fluctuations, and quasiperiodicity [17,43]. However, interesting doubts were cast on whether the Lang-Kobayashi model can predict the stable-unstable switching dynamics, which in recent experiments appeared to bifurcate from self-locking states as the feedback strengthens [12]. The model also needs to explain the expanded switching period that corresponds to a feedback-dependent frequency component slightly below $1/\tau$, as commonly observed in quasiperiodic laser dynamics [52–55].

In this paper, we examine the stable-unstable switching dynamics for a semiconductor laser under feedback. The Lang-Kobayashi model is first verified to produce the stable-unstable switching dynamics that practically bifurcates from the self-locking states, as the feedback strength $\xi$ increases for different delay times $\tau$. This clears the aforementioned doubts about the model in experiments [12]. Then, as $\xi$ increases, the Hopf boundary of MLM is derived and is found to match the boundaries of the stable-unstable switching regions. Moreover, in the instantaneous frequency-gain plane, the laser during the stable stage is analytically shown to follow the ellipse that contains the ECMs. Starting from the stable stage, the laser slowly moves around some stable ECMs between MGM and MLM. It then approaches the unstable ECMs that are destabilized by Hopf bifurcations, resulting in rapid oscillations near the relaxation resonance during the unstable stage. The laser subsequently returns to a stable ECM upon completing one switching period. Furthermore, we provide an analytical derivation of the switching period $\tau + \tau_\varepsilon$, where the expansion time $\tau_\varepsilon$ is found to be inversely proportional to the feedback strength $\xi$. The analytical results are in good agreement with the numerical results over a range of feedback parameters. The analysis explains the intriguing frequency downshifting from $1/\tau$ commonly observed in laser quasiperiodicity.

Following this Introduction, Sec. II presents the model for investigating the switching dynamics in Sec. III. The associated regions in the feedback parameter space are yielded numerically, while the analytical boundaries are derived in Sec. IV. The trajectory of the switching dynamics is analyzed in Sec. V. The expansion of the switching period $\tau + \tau_\varepsilon$ is analyzed in Sec. VI. The results are discussed in Sec. VII and summarized in Sec. VIII.

## II. RATE-EQUATION MODEL

Consider a laser under delayed optical feedback for invoking stable-unstable switching dynamics [12,13]. The laser is pumped by a bias current above threshold with a normalized value $\tilde{J}$ [15,56]. Light is reflected by a mirror for feedback with a round-trip delay time $\tau$, where a variable optical attenuator controls the feedback strength $\xi$ for the field. The complex intracavity electric field of the laser is $\sqrt{1+S(t)}\exp\left(i[\varphi(t)-\omega_0 t]\right)$. $S(t)$ is the optical intensity normalized with an offset to unity. $\varphi(t)$ is the optical phase so that the instantaneous angular frequency of the field is $\Omega(t) = -d\varphi/dt$, which is offset to the free-running optical angular frequency $\omega_0$. Moreover, the charge carriers in the laser provide an effective optical net gain $G(t)$ that includes the effects of cavity loss, imperfect overlap factor, and gain saturation by intracavity photons [27,57]. $G(t)$ is equal to the laser modal gain per unit time subtracted by the intracavity photon decay rate [32,58]. Based on the Lang-Kobayashi model, the dynamics of the laser is governed by the following rate equations for the normalized intensity $S$, optical phase $\varphi$, and gain $G$ [32,58]:

$$\frac{dS}{dt} = G(1+S) + 2\gamma_c\xi\sigma(1+S)\cos\Delta\varphi, \tag{1}$$

$$\frac{d\varphi}{dt} = -\frac{b}{2}G - \gamma_c\xi\sigma\sin\Delta\varphi, \tag{2}$$

$$\frac{dG}{dt} = -\gamma_r G - (\gamma_n+\gamma_p)SG - \Omega_r^2 S - 2\gamma_p\gamma_c\xi\sigma(1+S)\cos\Delta\varphi \tag{3}$$

with delayed phase difference $\Delta\varphi(t) = \varphi(t) - \varphi(t-\tau)$ and intensity ratio $\sigma^2(t) = [1+S(t-\tau)]/[1+S(t)]$, where $\Omega_r = \sqrt{\gamma_c\gamma_n + \gamma_s\gamma_p}$ is the relaxation resonance angular frequency and $\gamma_r = \gamma_s + \gamma_n + \gamma_p$ is the total carrier relaxation rate. The model is simplified by assuming a zero feedback phase, which corresponds to having the free-running frequency $\omega_0/2\pi$ at a multiple of $1/\tau$ [32,40]. The dynamical parameters are based on a laser used for communications: intracavity photon decay rate $\gamma_c = 536\ \mathrm{ns}^{-1}$, spontaneous carrier decay rate $\gamma_s = 5.96\ \mathrm{ns}^{-1}$, differential carrier relaxation rate $\gamma_n = 6.16\tilde{J}\ \mathrm{ns}^{-1}$, nonlinear carrier relaxation rate $\gamma_p = 15.6\tilde{J}\ \mathrm{ns}^{-1}$, and the linewidth enhancement factor $b = 3.2$, which quantifies the coupling of optical phase and intensity due to the antiguidance effect [15]. At $\tilde{J} = 1.222$, the relaxation resonance occurs at $\Omega_r/2\pi \approx 10$ GHz. The use of $\gamma_n$ and $\gamma_p$ follows the commonly adopted approximation of linearizing the gain function with respect to charge-carrier density and optical intensity [57–60]. When $\xi$ is zero, the steady-state solution of $(S, \Omega, G)$ is simply (0,0,0) for the free-running laser with continuous-wave emission at $\omega_0$. When $\xi$ is increased, the terms $\Delta\varphi(t)$ and $\sigma^2(t)$ give rise to the dynamics. Early works identified the importance of the fixed-point solutions, each corresponding to a continuous-wave emission at constant optical frequency and gain [29,49].

First, a fixed-point solution $(\Omega, G) = (\Omega_m, G_m)$ can be obtained from two equations:

$$\frac{1}{2}G_m + \gamma_c\xi\cos\Omega_m\tau = 0, \tag{4}$$

$$\Omega_m - \frac{b}{2}G_m + \gamma_c\xi\sin\Omega_m\tau = 0, \tag{5}$$

where the number $m$ is for labeling in ascending order of $\Omega_m$ [11,32]. Combining Eqs. (4) and (5) yields

$$\left(\Omega_m - \frac{b}{2}G_m\right)^2 + \left(\frac{1}{2}G_m\right)^2 = \gamma_c^2\xi^2, \tag{6}$$

which describes an ellipse in the angular frequency-gain plane of $(\Omega, G)$. For illustration, Fig. 1 shows such an ellipse for the fixed-point solutions when $\xi = 0.012$ and $\tau = 1.95$ ns. Similar ellipses have been reported in the plane of charge-carrier density and delayed phase difference in previous analyses and experiments, though this work focuses on the plane of $(\Omega, G)$ for clarity [11,61].

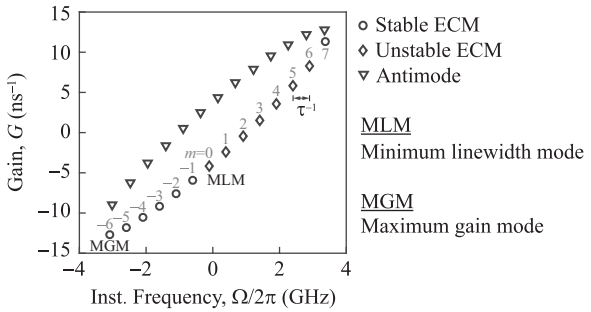


FIG. 1. Fixed-point solutions in the angular frequency-gain plane of ($\Omega$, $G$). The laser is subject to feedback of strength $\xi = 0.012$ and delay time $\tau = 1.95$ ns. The orders $m$ are labeled only for the ECMs.

Second, the fixed points are known to be created through saddle-node bifurcations because $\Omega_m$ can be found by eliminating $G_m$ from Eqs. (4) and (5) as [32]

$$\Omega_m + \sqrt{1+b^2}\,\gamma_c\xi\,\sin(\Omega_m\tau + \tan^{-1}b) = 0, \tag{7}$$

where the stability condition subject to phase fluctuations can be derived as [29]

$$\sqrt{1+b^2}\,\gamma_c\xi\,\cos(\Omega_m\tau + \tan^{-1}b + \pi) < 1/\tau, \tag{8}$$

which corresponds to differentiating with respect to the frequency. Each saddle-node bifurcation creates a pair of unstable and stable fixed-point solutions according to Eqs. (7) and (8). Here, while the solutions not satisfying Eq. (8) are called antimodes, the solutions satisfying Eq. (8) are regarded as ECMs and integers are assigned to $m$ as the orders of the ECMs [11]. When there are many ECMs, their angular frequencies are separated by about $2\pi/\tau$ [32]. So the number of ECMs is approximately [29]

$$M = \sqrt{1+b^2}\gamma_c\xi\tau/\pi. \tag{9}$$

The ECM with $\Omega_m$ being closest to zero is called MLM, as it provides strong damping on phase fluctuations in suppressing the linewidth, for which the order $m = 0$ is assigned conventionally [11,32]. The ECM with $G_m$ being minimal is called MGM, as it relies on the maximal gain compensation by feedback, for which the order $m$ is negative and $\Omega_m \approx -b\gamma_c\xi$ [12,62]. Illustrated in Fig. 1, the triangles on an upper side of the ellipse are the antimodes, while the other symbols on the lower part of the ellipse are the ECMs. Offset to the free-running optical frequency, MLM has a frequency of only $\Omega_0/2\pi = -0.1$ GHz, while MGM is at about $-3.1$ GHz with an order of $m = -6$.

Third, although an ECM always provides some damping to phase fluctuations, it can be destabilized by a supercritical Hopf bifurcation that stems from undamping the relaxation resonance between the photons and charge carriers [11,32]. A laser undergoing such a Hopf bifurcation becomes unstable in exhibiting periodic oscillations at a microwave angular frequency $\Omega_p$, which is typically very close to that of the relaxation resonance $\Omega_r$ in the long-cavity regime of $\Omega_r\tau \gg 2\pi$ [38]. Assuming that $|\Omega_p - \Omega_r| \ll \gamma_r$, the stability condition to avoid the Hopf bifurcation is given as [38]

$$\sqrt{1+b^2}\,\gamma_c\xi\,\cos(\Omega_m\tau - \tan^{-1}b - \pi) < \gamma_r/2 \tag{10}$$

for an ECM of order $m$. In Fig. 1, the unstable and stable ECMs are labeled as diamonds and circles, respectively. The ECMs are stable except for those with $m = 0$ to 6 in the example. In general, independent of the values of $\Omega_m$, the sufficient condition to ensure the stability for all ECMs can be simplified from Eq. (10) to [37,63]

$$\xi < \frac{\gamma_r}{2\gamma_c\sqrt{1+b^2}}, \tag{11}$$

which is useful for determining the stability boundaries in the feedback parameter space.

The Lang-Kobayashi model in Eqs. (1)–(3) is expressed for convenience using the gain $G$ rather than the charge-carrier density, which can be calculated from $G$ and $S$ [32,56]. Though the model contains no noise nor multiple reflections within the external cavity, it was well established by experiments [37,38]. Measurements of the emission intensity, phase, and charge-carrier density were recently demonstrated by photodetection, heterodyning, and probing the junction voltage [5,35]. The above summary about the fixed-point solutions enables the following analysis on the stable-unstable dynamics.

## III. STABLE-UNSTABLE SWITCHING

Figure 2 shows the stable-unstable switching for the laser in the route to chaos through carefully tuning the feedback strength $\xi$, while $\tau = 1.95$ ns, $\tilde{J} = 1.222$, and $b = 3.2$ are kept constant. Second-order Runge-Kutta integration is applied in Eqs. (1)–(3). For every point in the feedback parameter space ($\xi$, $\tau$), rather than allowing the dynamics to begin randomly, the simulation uses the free-running condition at $\xi = 0$ for initialization and then a sequential adjustment of $\xi$ in small incremental steps of $2 \times 10^{-4}$, where the complications of hysteresis associated with reducing $\xi$ are avoided [11]. For each step of $\xi$, the dynamics is simulated with a time step of 0.95 ps and a relatively long time span covering at least 2000 round-trips, which ensures the elimination of any residual transients [47]. Different from some numerical investigations, the above systematic procedure of simulation facilitates an improved comparison with experiments, where the feedback is in practice adjusted continually and slowly with respect to the laser dynamics [11,40].

Over a window of about $3\tau$, Fig. 2(i) shows the normalized intensity time series $S(t)$, while Fig. 2(ii) shows the associated optical spectrograms that are obtained using a short-time Fourier transform (STFT) on the complex field amplitude $\sqrt{1+S(t)}\exp(i\varphi(t))$. The spectrograms are offset to the free-running frequency of the laser for clarity. Each spectrogram is normalized to its maximum optical power with a sufficiently fine spectral resolution to reveal the dynamics, as a sufficiently long sliding Gaussian window of $4\pi/\Omega_r$ is adopted in the STFT. The spectrograms reveal the temporal evolution of the instantaneous optical spectra. They allow the identification of the dynamics [1]: A self-locking state is identified if the spectrum at any time has only a single peak that is at least 20 dB stronger than any residual sidebands. A periodic state

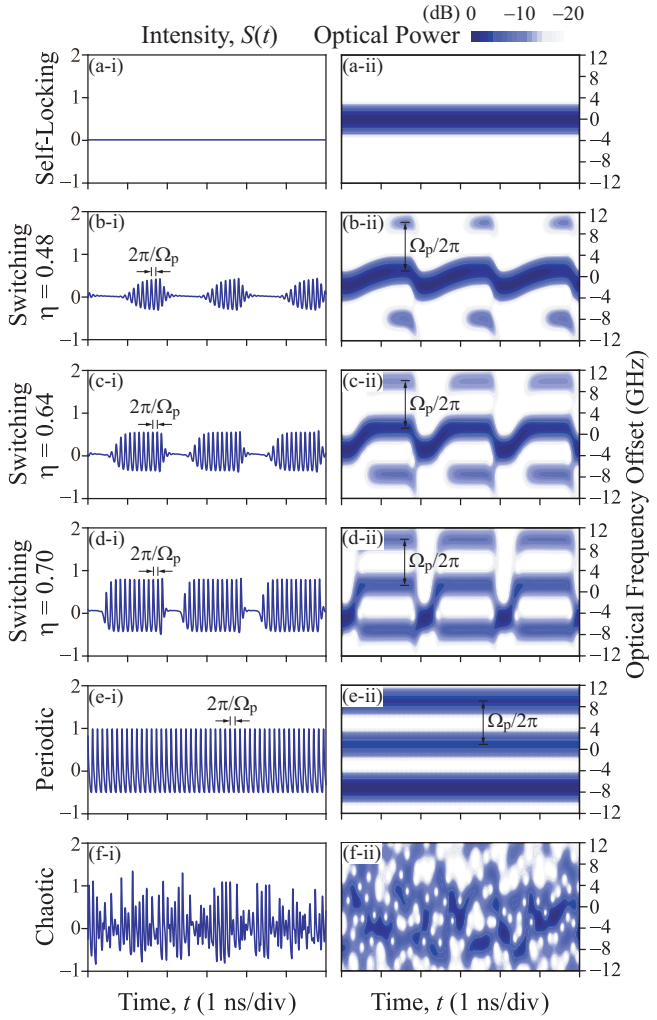


FIG. 2. (i) Normalized intensity $S(t)$ and (ii) optical spectrogram for the laser emitting in (a) the self-locking state, (b) switching dynamics with $\eta = 0.48$, (c) switching dynamics with $\eta = 0.64$, (d) switching dynamics with $\eta = 0.70$, (e) the periodic state, and (f) the chaotic state, where the feedback strength $\xi$ increases to 0.010, 0.012, 0.014, 0.018, 0.025, and 0.030, respectively. The feedback delay time is fixed at $\tau = 1.95$ ns.

is identified if the spectrum at any time has a main peak in association with strong side peaks, which are with comparable powers of within 20 dB and equally separated by the peak relaxation resonance frequency. Then, a stable-unstable switching dynamics is identified if the spectrum temporally alternates between that of a self-locking state and that of a periodic state, corresponding to a stable stage and an unstable stage of rapid intensity oscillations, respectively. Lastly, a dynamics is regarded as broadband and chaotic if the spectrum temporally fluctuates, where for over 20% of the time neither the self-locking spectrum nor the periodic spectrum is observed.

Figures 2(a)–2(f) are obtained as the feedback strength increases. Starting at $\xi = 0$ for a free-running laser, any increment of $\xi$ first results in self-locking at MLM that provides the best stability for the optical phase [38]. The general Hopf boundary in Eq. (11) is reached as $\xi$ increases to 0.009 and some ECMs can be destabilized, but MLM remains stable according to Eq. (10) at $m = 0$. For example, in Fig. 2(a) with $\xi = 0.010$, the laser stays in a self-locking state with emission at MLM that is stable under the feedback and has a small frequency of $\Omega_0/2\pi = -0.1$ GHz. The laser emits a stable intensity at its free-running value with $S(t) \approx 0$ in Fig. 2(a-i), while the associated optical spectrogram shows a single peak at any time in Fig. 2(a-ii).

By slightly tuning $\xi$ from 0.010 in Fig. 2(a) to 0.012 in Fig. 2(b), MLM becomes unstable because of a supercritical Hopf bifurcation. The laser is no longer self-locked by MLM in Fig. 2(a), but practically bifurcates into stable-unstable switching in Fig. 2(b) as the feedback strength is increased. Initially, for about 1.04 ns in the stable stage, the intensity $S(t)$ stays nearly constant in Fig. 2(b-i), and the optical spectrum in Fig. 2(b-ii) has only a single peak with a gradually increasing optical frequency. Then, for the next 0.96 ns in the unstable stage, the intensity rapidly oscillates in Fig. 2(b-i), and the spectrum in Fig. 2(b-ii) contains a main peak with side peaks, which are equally separated by a microwave oscillation frequency of $\Omega_p/2\pi \approx 9.1$ GHz near the relaxation resonance. Such stable-unstable switching repeats with a period of about 2.00 ns, where the unstable stage occupies a duty cycle $\eta$ of 0.48. Compared to the feedback delay time $\tau = 1.95$ ns, the switching period is slightly expanded, as exactly three switching periods are shown within 6.00 ns in Fig. 2(b). The stable-unstable switching is a form of quasiperiodicity for which the reciprocal of the switching period is incommensurate with the intensity oscillation frequency $\Omega_p/2\pi$.

As for $\xi = 0.014$ in Fig. 2(c), the stable-unstable switching dynamics continues with an increased duty cycle of $\eta = 0.64$. The unstable stage is lengthened in duration along with an increased amplitude of intensity oscillations according to $S(t)$ in Fig. 2(c-i), while the oscillation frequency $\Omega_p/2\pi$ remains nearly unchanged according to the spectrogram in Fig. 2(c-ii). At $\xi = 0.018$ in Fig. 2(d), these trends continue for the stable-unstable switching dynamics with an increased $\eta = 0.70$. Then, when $\xi$ increases to 0.025 in Fig. 2(e), the duty cycle $\eta$ ultimately reaches 1 as the laser enters a periodic state. The intensity is always unstably oscillating in Fig. 2(e-i), where the oscillation frequency $\Omega_p/2\pi$ is about 8 GHz according to the main peak and side peaks in the spectrogram in Fig. 2(e-ii) [64]. Finally, a slight increase of $\xi$ results in an abrupt change into chaotic states. An example is shown at $\xi = 0.030$ in Fig. 2(f) for the chaotically fluctuating intensity, which is accompanied by the time-varying broadband spectrum. Such a chaotic behavior continues when the feedback further strengthens [40].

The stable-unstable switching dynamics is observed as $\xi$ is adjusted over a fine range on the order of 0.01 in Fig. 2. The feedback strength for the stable-unstable switching dynamics cannot be too weak in entering the self-locking states nor too strong in entering the periodic or chaotic states [38,40]. The systematic simulation with the fine increment of $\xi$ with a long time span enables the practical observation of the stable-unstable switching that bifurcates from a self-locking state. Such an observation agrees with previously reported experiments [11,13]. It eliminates the earlier doubts about the validity of the Lang-Kobayashi model regarding the prediction of the switching dynamics [12].

## IV. SWITCHING REGIONS

Regions of the stable-unstable switching are investigated in the feedback parameter space in Fig. 3, following the procedures in Sec. III. Analytically, as MLM provides the best phase stability for the self-locking state, its stability with respect to the Hopf bifurcation is indicative of the boundary for stable-unstable switching. Considering $M \gg 1$ for the usual situations of having many ECMs, MLM has a small angular detuning frequency of

$$\Omega_0 \approx -\frac{\tan^{-1} b}{\tau} \tag{12}$$

from the free-running optical angular frequency $\omega_0$ according to Eq. (7). So based on Eq. (8), the Hopf stability condition of MLM becomes

$$\xi < \frac{\gamma_r \sqrt{1+b^2}}{2\gamma_c (b^2-1)} \tag{13}$$

for the usual case of $b > 1$, while the stability condition is always satisfied for $b < 1$. Compared to Eq. (11), which describes a sufficient condition for all ECMs to be stable, the Hopf stability condition in Eq. (13) is specific for MLM [37,38]. It provides a more accurate prediction for the boundaries between the self-locking regions and the stable-unstable switching regions as detailed below.

Figure 3 shows the mappings of the different laser dynamics in the parameter space of feedback strength $\xi$ versus feedback delay time, bias current, and linewidth enhancement factor. Regions are found for the self-locking states (white), stable-unstable switching (light blue), periodic states (dark blue), and chaotic states (black). In Fig. 3, the regions for the stable-unstable switching dynamics are shown in light blue, where the scaled colors with the contour lines show the duty cycle $\eta$ of the unstable stage. For the white regions of self-locking states, $\xi$ is small and the laser stays in MLM because of its maximal stability for the optical phase. The general Hopf bifurcation boundaries for $\xi$ in Eq. (11) are shown as the gray curves. However, for destabilizing MLM, the specific Hopf bifurcation boundaries for $\xi$ in Eq. (13) should be used instead. Such MLM Hopf boundaries are shown as the red curves. Clearly, regions in light blue for the stable-unstable switching dynamics are found for $\xi$ exceeding the specific Hopf bifurcation boundaries for MLM. As $\xi$ increases, the duty cycle $\eta$ generally increases from 0 within the regions of stable-unstable switching. Additionally, there are very small regions of periodic states in dark blue that correspond to $\eta = 1$, but they are next to the large regions of broadband and chaotic states in black at the relatively strong $\xi$. Thus, Fig. 3 illustrates the route to chaos consisting of the self-locking states, stable-unstable switching as a form of quasiperiodicity, and also periodic states. The specific Hopf bifurcation condition for MLM in Eq. (13) corresponds to the boundaries for the stable-unstable switching with $\eta \approx 0$.

For Fig. 3(a), the dynamical regions are obtained for $\xi$ versus the normalized feedback delay time $\tilde{\tau} = \tau\Omega_r/2\pi$, while keeping $\tilde{J} = 1.222$ and $b = 3.2$. Stable-unstable switching dynamics is found only in the long-cavity regime with $\tilde{\tau} \gg 1$, which agrees with experiments [13,36]. As shown in light blue, a region for the switching dynamics is bounded by

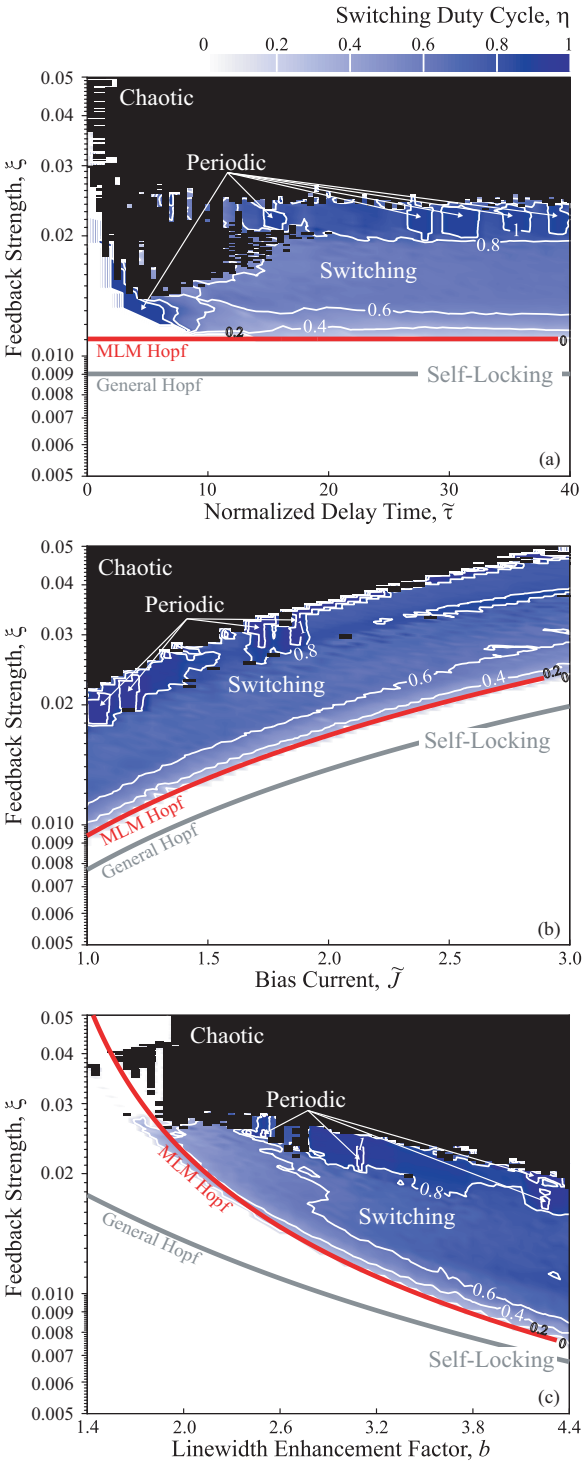


FIG. 3. Regions of the laser dynamics in the parameter space of feedback strength $\xi$ vs (a) normalized delay time $\tilde{\tau}$, (b) normalized bias current $\tilde{J}$, and (c) linewidth enhancement factor $b$. The laser is in a self-locking state (white), stable-unstable switching (light blue), a periodic state (dark blue), and a chaotic state (black). The switching dynamics comprises a stable stage and an unstable stage with a duty cycle of $\eta$ (contour lines). The gray curves are the Hopf bifurcation boundaries for any ECMs in general according to Eq. (11). The red curves are the Hopf bifurcation boundaries specific to MLM according to Eq. (13).

$\xi = 0.011$, which coincides with the specific Hopf boundary for MLM in Eq. (13) as the red curve presents. The duty cycle $\eta$ increases with $\xi$ as the laser leaves the self-locking region in approaching the chaotic region. For Fig. 3(b), while fixing $\tilde{\tau} = 20$ and $b = 3.2$, the mapping is obtained for $\xi$ versus $\tilde{J}$ for the normalized current biased above threshold. As an operational parameter, the current can be easily adjusted for varying the dynamical parameters $\gamma_n$ and $\gamma_p$, which results in the tuning of $\Omega_r$ and $\gamma_r$ of the relaxation resonance. So both the general and specific Hopf boundaries of $\xi$ increase with $\tilde{J}$ according to Eqs. (11) and (13). Stable-unstable switching dynamics is again found in a region above the specific Hopf boundary in red for MLM. As for Fig. 3(c), while fixing $\tilde{\tau} = 20$ and $\tilde{J} = 1.222$, the dynamical regions are obtained for $\xi$ versus the linewidth enhancement factor $b$. Both the general and specific Hopf boundaries by Eqs. (11) and (13) show the increment of $\xi$ as $b$ is reduced. Reducing $b$ is commonly known for suppressing nonlinear dynamics [37]. As far as $b$ is greater than 2, stable-unstable switching can be found in a region above the specific Hopf boundary in red for MLM using Eq. (13).

Based on Fig. 3, stable-unstable switching is in practice found to bifurcate from a self-locking state. The regions of stable-unstable switching are generally bounded by the specific Hopf condition in Eq. (13), where the duty cycle $\eta$ for the unstable stage increases with $\xi$.

## V. SWITCHING TRAJECTORY

The switching dynamics is investigated using the trajectory in the plane of instantaneous angular frequency $\Omega(t)$ and gain $G(t)$. As mentioned in Sec. III, the switching period is slightly expanded from $\tau$. The switching period is now denoted as $\tau + \tau_\varepsilon$ to include the period expansion time $\tau_\varepsilon$. For analyzing the trajectory, $\Omega(t)$ is approximated as perfectly periodic in $\tau + \tau_\varepsilon$, so the phase $\varphi(t)$ changes accumulatively by a constant of

$$\theta = -\int_0^{\tau+\tau_\varepsilon} \Omega(t)dt \tag{14}$$

for every period of stable-unstable switching. During the stable stage, except for a narrow time window of $\tau_\varepsilon$ immediately before the stage ends, $dS(t)/dt$ vanishes and $S(t) = S(t + \tau_\varepsilon)$, which equals $S(t - \tau)$ because $S(t)$ is also periodic in $\tau + \tau_\varepsilon$. As a result, $\sigma(t) = 1$ and $\Delta\varphi(t)$ can be eliminated in Eqs. (1) and (2) to yield

$$\left(\Omega(t) - \frac{b}{2}G(t)\right)^2 + \left(\frac{1}{2}G(t)\right)^2 = \gamma_c^2\xi^2, \tag{15}$$

which is an equation for an ellipse as in Eq. (6). Thus, although not staying in a particular ECM at $(\Omega_m, G_m)$, the time-varying trajectory $[\Omega(t), G(t)]$ should follow the ellipse of Eq. (15) during the stable stage. In other words, the ellipse is applicable to not only the usual self-locking states but also the switching dynamics [3,12].

Numerically, focusing on one complete switching period, the trajectory of the stable-unstable switching dynamics is examined in detail in Figs. 4 and 5. The laser is subject to feedback of strength $\xi = 0.012$ and delay time $\tau = 1.95$ ns as in Fig. 2(b). The switching dynamics repeats with a period of $\tau + \tau_\varepsilon = 2.00$ ns with $\tau_\varepsilon = 0.05$ ns. The switching period

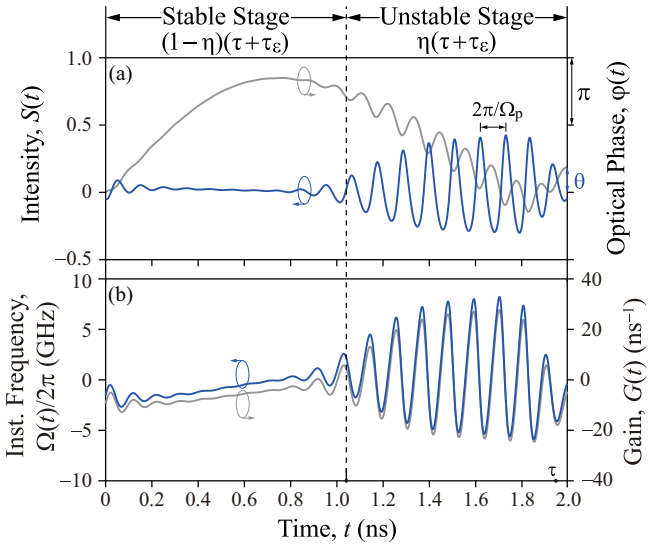


FIG. 4. Normalized intensity $S(t)$, optical phase $\varphi(t)$, instantaneous frequency $\Omega(t)/2\pi$, and gain $G(t)$ in one period of stable-unstable switching. The switching period is $\tau + \tau_\varepsilon = 2.00$ ns with an expansion time of $\tau_\varepsilon = 0.05$ ns. The duty cycle for the unstable stage is $\eta = 0.48$. Feedback parameters are $(\xi, \tau) = (0.012, 1.95$ ns).

contains the stable stage for $0 < t < 1.04$ ns and the unstable stage for $1.04$ ns $< t < 2.00$ ns in correspondence to a duty cycle of $\eta = 0.48$. The switching period is clearly longer than $\tau$ as Fig. 4 shows. In Fig. 4(a), the normalized intensity in blue shows a nearly constant value at $S(t) \approx 0$ for $t = 0$ to $(1 - \eta)(\tau + \tau_\varepsilon)$ during the stable stage, followed by the rapid unstable oscillations with a period of $2\pi/\Omega_p$ and a full amplitude of about 0.7 during the unstable stage. The laser returns to the stable stage upon completion of a switching period of $\tau + \tau_\varepsilon = 2.00$ ns. The corresponding optical phase $\varphi(t)$ in gray shows a gradual increment during the stable stage, followed again by some rapid oscillations with a successive reduction during the unstable stage. In Fig. 4(b), by taking the time derivative on $-\varphi(t)$, the instantaneous angular frequency $\Omega(t)$ as offset from $\omega_0$ is obtained. During the stable stage, the instantaneous frequency in blue is mostly negative, as it starts at around $-2$ GHz and increases nearly linearly at a rate of about 3 GHz/ns. Rapid oscillations between $-6$ and 8 GHz are then observed during the unstable stage. The corresponding temporal variation of the gain $G(t)$ in gray resembles that of $\Omega(t)$, although the details can be better examined in the plane of $(\Omega, G)$.

Over one complete period $\tau + \tau_\varepsilon$ of stable-unstable switching, Fig. 4 shows that the intensity $S(t)$, instantaneous frequency $\Omega(t)/2\pi$, and gain $G(t)$ basically return to their respective initial values, while the phase $\varphi(t)$ increases by $\theta \approx 1.2$ rad as labeled. Interestingly, in a narrow time window of $\tau_\varepsilon$ immediately before the stable-to-unstable switching at $t = (1 - \eta)(\tau + \tau_\varepsilon)$, the phase difference $\Delta\varphi(t)$ compares $\varphi(t)$ in the current stable stage to $\varphi(t - \tau)$, which is at time $-\eta(\tau + \tau_\varepsilon) + \tau_\varepsilon$ in the previous unstable stage. In fact, the term $\varphi(t - \tau)$ in the rate equations brings the rapid variations during the previous unstable stage for switching the current stable stage into the unstable stage [32]. Thus, the nonzero

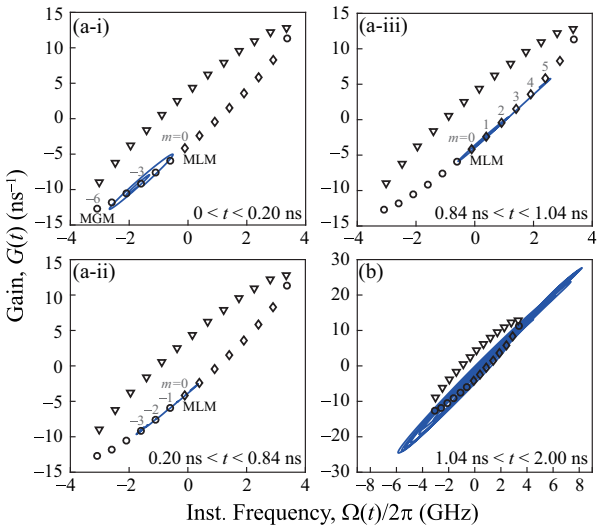


FIG. 5. Trajectories in the plane of $(\Omega, G)$ in one period of stable-unstable switching, including (a) the stable stage for $0 < t < 1.04$ ns and (b) the unstable stage for 1.04 ns $< t <$ 2.00 ns. The stable stage is further divided into subplots (i), (ii), and (iii) for clarity in confirming Eq. (15). Feedback parameters are $(\xi, \tau) = (0.012, 1.95$ ns).

expansion time $\tau_\varepsilon$ is essential for the stable-unstable switching.

Figure 5 further presents the trajectory in the angular frequency-gain plane $(\Omega, G)$. The stable ECMs, unstable ECMs, and antimodes are denoted by circles, diamonds, and triangles, respectively, as in Fig. 1. Starting at $t = 0$, Fig. 5(a-i) shows over a transient of about 0.20 ns that the trajectory spirals into the stable ECM of $m = -3$, which is between MGM and MLM. As the stable stage continues in Fig. 5(a-ii) for 0.20 ns $< t <$ 0.84 ns, the trajectory slowly migrates along the lower part of the ellipse in Eq. (15), while visiting the stable ECMs of $m = -2$ and $-1$. At about 0.84 ns in Fig. 5(a-iii), the stable stage is about to end as the trajectory approaches MLM of $m = 0$. MLM is unstable so that the trajectory quickly moves to a few other ECMs of up to $m \approx 5$ at $t = 1.04$ ns. Lastly, in Fig. 5(b), the trajectory exhibits rapid oscillations with large variations of $(\Omega, G)$ for 1.04 ns $< t <$ 2.00 ns during the unstable stage.

In the plane of $(\Omega, G)$, Fig. 5 complements different early investigations about the portraits of carrier density or the delayed phase difference [32]. The trajectory in Fig. 5 directly illustrates the behaviors of the instantaneous frequency and gain experienced by the laser light. Agreeing with Eq. (15), the trajectory in Figs. 5(a-i)–5(a-iii) confirms that the laser visits several ECMs around MLM during the stable stage, where the lower part of the ellipse is followed.

## VI. SWITCHING PERIODICITY

While Fig. 4 specifically shows one switching period, the value of the period expansion time $\tau_\varepsilon$ can be more accurately determined by consecutively observing a large number of switching periods in Figs. 6 and 7. To analytically obtain the expansion time, the periodicity of $\Omega(t)$ in $\tau + \tau_\varepsilon$ is used to express

$$\Delta\varphi(t) = \varphi(t) - \varphi(t + \tau_\varepsilon) + \theta, \tag{16}$$

where $\theta$ from Eq. (14) is the phase change accumulated in one switching period. During the stable stage, there are no rapid changes of $\Omega(t)$ and so

$$\Delta\varphi(t) \approx \theta + \tau_\varepsilon \Omega(t) \tag{17}$$

except for a narrow time window of $\tau_\varepsilon$ immediately before every stable-to-unstable switch. Substituting $\Delta\varphi(t)$ in Eq. (17) into the rate equation of Eq. (2) yields

$$\Omega(t) - \frac{b}{2} G(t) - \gamma_c \xi \sin(\theta + \tau_\varepsilon \Omega(t)) = 0, \tag{18}$$

which governs the trajectory in the plane of $(\Omega, G)$.

The trajectory in Eq. (18) cannot be perfectly fitted to the ellipse in Eq. (15), but it can be fitted to a specific point and slope on the ellipse. Due to the proximity to MLM, the point at $\Omega = 0$ on the lower part of the ellipse is chosen for which $G = -2\gamma_c \xi / \sqrt{1 + b^2}$ with an associated slope of $G' = 2b/(1 + b^2)$, according to Eq. (15). Therefore, the fitting of Eqs. (15) and (18) at $\Omega = 0$ yields the expansion time of

$$\tau_\varepsilon = \frac{1}{\sqrt{1 + b^2}\gamma_c \xi} \tag{19}$$

as a major result of the analysis. The period expansion from $\tau$ explains the frequency component that is slightly lower than $1/\tau$ in quasiperiodic laser dynamics [11,32]. The fitting also yields the accumulated phase of

$$\theta = \tan^{-1} b - 2\pi n \tag{20}$$

for some integer $n$. The results derived in Eqs. (19) and (20) are based on requiring the trajectory in Eq. (18) to follow the ellipse in the plane of $(\Omega, G)$, where MLM and the neighboring ECMs are visited. Such a requirement is consistent with the fact that the stable ECMs have basins of attraction. The migration of the laser between the ECMs is confirmed numerically in Fig. 5 and analytically in Eq. (15).

For simplicity, by recalling $M$ in Eq. (9) for the number of ECMs, Eq. (19) can be rewritten as $\tau_\varepsilon = \tau/\pi M$. Additionally, Eq. (20) yields the time-averaged optical angular frequency as

$$\langle \Omega(t) \rangle = \frac{-\tan^{-1} b + 2\pi n}{\tau + \tau_\varepsilon}, \tag{21}$$

which is obtained through dividing the accumulated phase $\theta$ by the switching period $\tau + \tau_\varepsilon$. For the usual case involving a large number of ECMs $M$, $\tau_\varepsilon \ll \tau$ and so Eq. (21) becomes $\langle \Omega \rangle = -\tan^{-1} b/\tau$ for $n = 0$, which matches the frequency of MLM in Eq. (12). As for a nonzero $n$, $\langle \Omega \rangle$ matches an ECM of order $m = n$. Thus, despite the stable-unstable switching dynamics, the laser emission is still on average at MLM or at an ECM.

Numerically, for clearly determining the periodicity of the stable-unstable switching, Fig. 6 presents the intensity, frequency, and gain using space-time plots in $(r, N)$, where time $t = (N + r)(\tau + \tau_\varepsilon)$ for $r$ in [0, 1), and $N$ is an integer. Because $\tau_\varepsilon$ is much smaller than $\tau$, $r$ is interpreted as the space coordinate in the external cavity, whereas $N$ denotes the number of periods [4,53]. As in Figs. 4 and 5 with $\eta = 0.48$, the parameters are kept as $\xi = 0.012$ and $\tau = 1.95$ ns in Fig. 6. Figure 6 shows that the expansion time $\tau_\varepsilon$ has to be set at 0.05 ns in order to keep the boundary between stable and unstable stages independent of $N$, where the boundary is

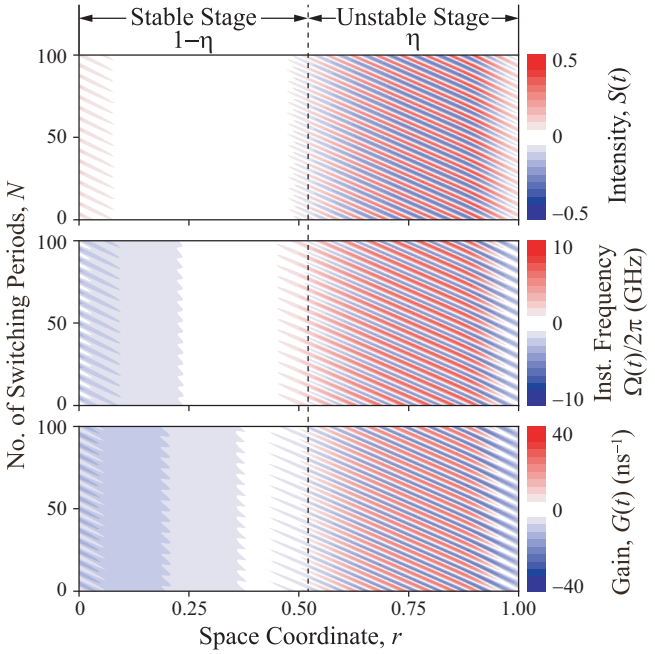


FIG. 6. Normalized intensity $S$, instantaneous frequency $\Omega/2\pi$, and gain $G$ of stable-unstable switching as space-time plots of $(r, N)$, where $r$ is the space coordinate and $N$ is the number of switching periods. Each switching period is $\tau + \tau_\varepsilon = 2.00$ ns. Feedback parameters are $(\xi, \tau) = (0.012, 1.95\ \text{ns})$.

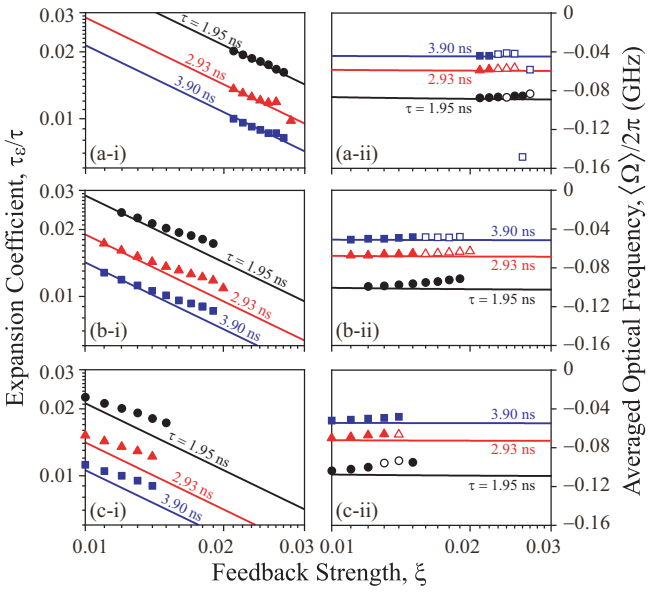


FIG. 7. (i) Switching period expansion coefficient $\tau_\varepsilon/\tau$ and (ii) averaged optical frequency $\langle\Omega\rangle/2\pi$ for the stable-unstable switching dynamics as functions of $\xi$ for $\tau = 1.95$ ns (black), 2.93 ns (red), and 3.90 ns (blue), where $b =$ (a) 2.0, (b) 3.2, and (c) 4.4. Numerical results are in closed symbols, while the corresponding analytical curves are from Eqs. (19) and (21) with $n = 0$. For completeness, the open symbols are numerical results of $\langle\Omega\rangle/2\pi$ shifted for comparison with Eq. (21).

located at $r = 0.52$ in correspondence to $1 - \eta$. The stable spatial region in $0 < r < 1 - \eta$ contains a nearly constant $S \approx 0$ with only gradual and small changes of $\Omega$ and $G$. The unstable spatial region in $1 - \eta < r < 1$ contains about nine rapid oscillations with large amplitudes for $S$, $\Omega$, and $G$ at any fixed $N$. There are slanted stripes corresponding to a minor change of the microwave phase of oscillation in every increment of $N$, but the microwave phase change is only about $0.28\pi$ and is ignored in the analysis for simplicity. In brief, the separate spatial regions of stable and unstable dynamics are essentially independent of $N$ in Fig. 6, which confirms the approximations of $S(t)$, $\Omega(t)$, and $G(t)$ as periodic functions in $\tau + \tau_\varepsilon$.

To verify the analytical results in Eqs. (19) and (21), Fig. 7 presents the numerical results obtained from accurately determining an expansion coefficient $\tau_\varepsilon/\tau$ and the averaged optical frequency $\langle\Omega\rangle/2\pi$, which are based on long-term simulations using a large $N$ on the order of $10^3$. For comparison, the analytical results from Eqs. (19) and (21) are shown by the curves. The numerical results are shown by the closed symbols for the ranges of $\xi$ that yield the stable-unstable switching dynamics, where the black circles, red triangles, and blue squares are for $\tau = 1.95$, 2.93, and 3.90 ns, respectively. The simulations are conducted in rows (a), (b), and (c) for $b = 2.0$, 3.2, and 4.4, respectively. Column (i) in Fig. 7 shows the expansion coefficient $\tau_\varepsilon/\tau$ of the switching period. The stable-unstable dynamics is observed within different ranges of $\xi$ as marked by the numerical data points. The numerical results and the analytical results of Eq. (19) are generally in good agreement, despite some small deviations for large $\xi$ near the chaotic regions. The results show a continuous reduction of $\tau_\varepsilon$ as $\xi$ strengthens. Column (ii) in Fig. 7 shows the averaged optical frequency $\langle\Omega\rangle/2\pi$ for the stable-unstable switching dynamics. For small $\xi$ within the ranges of inducing the switching dynamics, the closed symbols from the numerical simulations closely match the analytical curves from Eq. (21) with $n = 0$. Thus, long-term averaged over many switching periods, the laser under stable-unstable dynamics simply emits at the frequency of MLM. As for a relatively large $\xi$, the averaged frequency $\langle\Omega\rangle/2\pi$ can jump to different values, while the open symbols show the values offset by multiples of $1/(\tau + \tau_\varepsilon)$ with $\tau_\varepsilon$ obtained from Eq. (19). The open symbols again match the analytical curves of Eq. (21), indicating the emissions at an ECM when time-averaged, though further increasing $\xi$ drives the laser into chaos.

Overall, Fig. 7 shows the good agreement between the numerical results and the analytical results in Eqs. (19) and (21). The laser tends to remain in MLM when averaged over many switching periods. The results indicate the importance of MLM on the laser dynamics. The expansion time $\tau_\varepsilon$, representing the reaction time of the laser in responding to the feedback light, is numerically and analytically confirmed as inversely proportional to $\xi$.

## VII. DISCUSSIONS

In relation to the previous experiments [12], the detailed behaviors around the onset of switching dynamics are examined in Fig. 8, where the oscillation amplitude of $S(t)$ is plotted along with $\eta$ over a narrow range of $\xi$. The oscillation amplitude is recorded as half of the peak-to-peak value of $S(t)$. The feedback delay time is fixed at 1.95 ns. The top row of

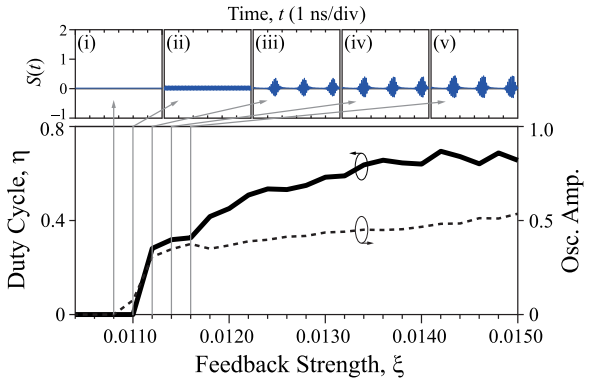


FIG. 8. Duty cycle and oscillation amplitude recorded as $\xi$ is increased over a narrow range near the onset of switching. Top row: $S(t)$ for $\xi =$ (i) 0.0108, (ii) 0.0110, (iii) 0.0112, (iv) 0.0114, and (v) 0.0116. The oscillation and then the switching both begin within an extremely narrow range of $\xi$ from 0.0108 to 0.0112, which is merely a 3.7% relative change.

Fig. 8 records some very fine details of the dynamics between those in Figs. 2(a) and 2(b). For $\xi$ up to 0.0108 in Fig. 8(i), the laser is self-locked at MLM, which is in accordance with Fig. 3(a). For $\xi$ of 0.0110 in Fig. 8(ii), the boundary in Eq. (13) is reached for a supercritical Hopf bifurcation of MLM, where $S(t)$ begins to oscillate periodically with a small amplitude of less than 0.07. The small-amplitude oscillation is very weak when compared to the large-amplitude oscillation for the periodic state in Fig. 2(e-i). It is still numerically identified as a self-locking state rather than a periodic state, which is because its optical spectrum has only very weak side peaks of less than $-20$ dB of the main peak. As for $\xi$ of 0.0112 in Fig. 8(iii), the stable-unstable switching dynamics begins, while the oscillation amplitude is much boosted to 0.31. Further increasing $\xi$ gives continual increments of the duty cycle and oscillation amplitude in Figs. 8(iv) and 8(v).

In Fig. 8, the dashed curve for the oscillation amplitude rises from zero when $\xi$ is increased beyond the Hopf bifurcation boundary. The solid curve for the switching duty cycle also rises as $\xi$ increases. The two curves start to rise at nearly the same $\xi$ of between 0.0108 to 0.0112. In other words, the Hopf bifurcation and then the switching begin within the extremely narrow range of 0.0004 for $\xi$, which corresponds to a relative change of merely 3.7%. Such a range of $\xi$ is too narrow for developing a sufficiently large periodic oscillation amplitude for identifying with a periodic state. The switching dynamics thus appears to practically bifurcate from the self-locking state, as illustrated in Sec. III. The extremely narrow range of $\xi$ and the small amplitude of oscillations are probably the reasons for not observing any periodic oscillations immediately before the onset of switching in experiments [12].

Moreover, in relating to other photonic systems, the result in Eq. (19) sheds important light on the repeated stable-unstable switching dynamics. There is always an expansion of the switching period, where the expansion time $\tau_\varepsilon$ is inversely proportional to $\xi$. This corresponds to the generation of the feedback-dependent frequency downshifted from $1/\tau$ as commonly observed in quasiperiodic dynamics of lasers [32,55]. The period expansion has been noted as drifts of the switching period in early works on laser dynamics [33,53]. More recently, in the context of cavity solitons, such a period expansion by a time inversely proportional to the feedback strength was also observed in the study of temporal dissipative localized states [65,66]. Similar drifts have been observed in the spatiotemporal dynamics for chimeras and reservoir computing in lasers under feedback [18,67], optoelectronic oscillators [68], mode-locked lasers [69,70], and edge-emitting lasers with polarization-rotated feedback [71,72]. Though the period expansion is often attributed to some general internal reaction times of the lasers, the result in Eq. (19) offers a quantitative explanation for the stable-unstable switching for extensions to other dynamics in the future.

## VIII. CONCLUSION

To conclude, the stable-unstable switching dynamics is thoroughly investigated for the semiconductor laser under optical feedback. Contrary to the recent doubts, the Lang-Kobayashi model is first verified to produce the switching dynamics that practically bifurcates from the self-locking states when the feedback strengthens, as is consistent with previous experiments [12]. Then, the analytical Hopf boundary of MLM is derived in matching the boundaries of the switching regions in the feedback parameter space in Eq. (13). Moreover, during the stable stage, the laser is analytically shown to follow the ellipse of ECMs in Eq. (15) while migrating around some stable ECMs between MGM and MLM in the plane of $(\Omega, G)$. Finally, as the trajectory follows the ellipse near MLM, the switching period expansion time $\tau_\varepsilon$ is analytically derived in Eq. (19) to be inversely proportional to the feedback strength $\xi$. The period expansion explains the general observation of a shifted frequency component slightly below $1/\tau$ in quasiperiodic laser dynamics. While further analyzing the more complicated spatiotemporal behavior is possible, the results essentially contribute to harnessing the switching dynamics in photonic microwave generation.

## ACKNOWLEDGMENTS

The work described in this paper was fully supported by the grants from the Research Grants Council of Hong Kong, China (Projects No. CityU 11200618, No. CityU 11204519, and No. T42-103/16-N).

[1] T. B. Simpson, J. M. Liu, M. AlMulla, N. G. Usechak, and V. Kovanis, Phys. Rev. Lett. **112**, 023901 (2014).
[2] M. Sciamanna and K. A. Shore, Nat. Photon. **9**, 151 (2015).
[3] M. C. Soriano, J. Garcia-Ojalvo, C. R. Mirasso, and I. Fischer, Rev. Mod. Phys. **85**, 421 (2013).
[4] C. H. Uy, L. Weicker, D. Rontani, and M. Sciamanna, APL Photon. **4**, 056104 (2019).
[5] C. Y. Chang, D. Choi, A. Locquet, M. J. Wishon, K. Merghem, A. Ramdane, F. Lelarge, A. Martinez, and D. S. Citrin, Appl. Phys. Lett. **108**, 191109 (2016).

[6] C. H. Tseng, Y. H. Hung, and S. K. Hwang, Opt. Lett. **44**, 3334 (2019).

[7] L. Zhang and S. C. Chan, Opt. Lett. **44**, 4905 (2019).

[8] T. B. Simpson, J. M. Liu, M. AlMulla, N. G. Usechak, and V. Kovanis, IEEE J. Sel. Top. Quantum Electron. **19**, 1500807 (2013).

[9] J. P. Zhuang and S. C. Chan, Opt. Lett. **38**, 344 (2013).

[10] C. Y. Chang, M. J. Wishon, D. Choi, J. Dong, K. Merghem, A. Ramdane, F. Lelarge, A. Martinez, A. Locquet, and D. S. Citrin, IEEE J. Quantum Electron. **53**, 2000406 (2017).

[11] A. Locquet, B. Kim, D. Choi, N. Li, and D. S. Citrin, Phys. Rev. A **95**, 023801 (2017).

[12] M. J. Wishon, A. Locquet, C. Y. Chang, D. Choi, and D. S. Citrin, Phys. Rev. A **97**, 033849 (2018).

[13] J. X. Dong, J. P. Zhuang, and S. C. Chan, Opt. Lett. **42**, 4291 (2017).

[14] A. Uchida, K. Amano, M. Inoue, K. Hirano, S. Naito, H. Someya, I. Oowada, T. Kurashige, M. Shiki, S. Yoshimori, K. Yoshimura, and P. Davis, Nat. Photon. **2**, 728 (2008).

[15] X. Z. Li, J. P. Zhuang, S. S. Li, J. B. Gao, and S. C. Chan, Phys. Rev. E **94**, 042214 (2016).

[16] N. Li, H. Susanto, B. R. Cemlyn, I. D. Henning, and M. J. Adams, Phys. Rev. A **96**, 013840 (2017).

[17] A. Karsaklian Dal Bosco, N. Sato, Y. Terashima, S. Ohara, A. Uchida, T. Harayama, and M. Inubushi, IEEE J. Sel. Top. Quantum Electron. **23**, 1801208 (2017).

[18] L. Appeltant, M. C. Soriano, G. Van der Sande, J. Danckaert, S. Massar, J. Dambre, B. Schrauwen, C. R. Mirasso, and I. Fischer, Nat. Commun. **2**, 468 (2011).

[19] D. Brunner, M. C. Soriano, C. R. Mirasso, and I. Fischer, Nat. Commun. **4**, 1364 (2013).

[20] C. Sugano, K. Kanno, and A. Uchida, IEEE J. Sel. Top. Quantum Electron. **26**, 1500409 (2020).

[21] A. Argyris, D. Syvridis, L. Larger, V. Annovazzi-Lodi, P. Colet, I. Fischer, J. Garcia-Ojalvo, C. R. Mirasso, L. Pesquera, and K. A. Shore, Nature **438**, 343 (2005).

[22] V. Annovazzi-Lodi and G. Aromataris, IEEE J. Quantum Electron. **51**, 7000405 (2015).

[23] H. L. Tsay, C. Y. Wang, J. D. Chen, and F. Y. Lin, Opt. Express **28**, 24037 (2020).

[24] L. C. Lin, S. H. Liu, and F. Y. Lin, Opt. Express **25**, 25523 (2017).

[25] C. H. Tseng and S. K. Hwang, Opt. Lett. **45**, 3777 (2020).

[26] B. Nie, Y. Ruan, Y. Yu, Q. Guo, J. Xi, and J. Tong, J. Lightwave Technol. **38**, 5423 (2020).

[27] R. Lang and K. Kobayashi, IEEE J. Quantum Electron. **16**, 347 (1980).

[28] J. Mork, J. Mark, and B. Tromborg, Phys. Rev. Lett. **65**, 1999 (1990).

[29] J. Mork, B. Tromborg, and J. Mark, IEEE J. Quantum Electron. **28**, 93 (1992).

[30] A. Ritter and H. Haug, J. Opt. Soc. Am. B **10**, 145 (1993).

[31] I. Fischer, G. H. M. van Tartwijk, A. M. Levine, W. Elsasser, E. Gobel, and D. Lenstra, Phys. Rev. Lett. **76**, 220 (1996).

[32] C. Masoller and N. B. Abraham, Phys. Rev. A **57**, 1313 (1998).

[33] T. Erneux, A. Gavrielides, and M. Sciamanna, Phys. Rev. A **66**, 033809 (2002).

[34] B. Dong, J. D. Chen, F. Y. Lin, J. C. Norman, J. E. Bowers, and F. Grillot, Phys. Rev. A **103**, 033509 (2021).

[35] D. Brunner, M. C. Soriano, X. Porte, and I. Fischer, Phys. Rev. Lett. **115**, 053901 (2015).

[36] B. Kim, A. Locquet, D. Choi, and D. S. Citrin, Phys. Rev. A **91**, 061802(R) (2015).

[37] F. Grillot, C. Wang, N. A. Naderi, and J. Even, IEEE J. Sel. Top. Quantum Electron. **19**, 1900812 (2013).

[38] D. Lenstra, T. T. M. van Schaijk, and K. A. Williams, IEEE J. Sel. Top. Quantum Electron. **25**, 1502113 (2019).

[39] S. Donati and R. H. Horng, IEEE J. Sel. Top. Quantum Electron. **19**, 1500309 (2013).

[40] S. S. Li and S. C. Chan, IEEE J. Sel. Top. Quantum Electron. **21**, 1800812 (2015).

[41] T. Harayama, S. Sunada, K. Yoshimura, J. Muramatsu, K. I. Arai, A. Uchida, and P. Davis, Phys. Rev. E **85**, 046215 (2012).

[42] X. Porte, M. C. Soriano, and I. Fischer, Phys. Rev. A **89**, 023822 (2014).

[43] D. Brunner, X. Porte, M. C. Soriano, and I. Fischer, Sci. Rep. **2**, 732 (2012).

[44] T. Heil, I. Fischer, W. Elsasser, and A. Gavrielides, Phys. Rev. Lett. **87**, 243901 (2001).

[45] A. Tabaka, K. Panajotov, I. Veretennicoff, and M. Sciamanna, Phys. Rev. E **70**, 036211 (2004).

[46] A. Karsaklian Dal Bosco, Y. Akizawa, K. Kanno, A. Uchida, T. Harayama, and K. Yoshimura, Opt. Express **24**, 22198 (2016).

[47] D. Choi, M. J. Wishon, C. Y. Chang, D. S. Citrin, and A. Locquet, Chaos **28**, 011102 (2018).

[48] M. J. Wishon, D. Choi, T. Niebur, N. Webster, Y. K. Chembo, E. A. Viktorov, D. S. Citrin, and A. Locquet, IEEE Photon. Technol. Lett. **30**, 1597 (2018).

[49] A. Ritter and H. Haug, J. Opt. Soc. Am. B **10**, 130 (1993).

[50] S. G. Abdulrhmann, M. Ahmed, T. Okamoto, W. Ishimori, and M. Yamada, IEEE J. Sel. Top. Quantum Electron. **9**, 1265 (2003).

[51] K. Petermann, IEEE J. Sel. Top. Quantum Electron. **1**, 480 (1995).

[52] P. M. Alsing, V. Kovanis, A. Gavrielides, and T. Erneux, Phys. Rev. A **53**, 4429 (1996).

[53] C. Masoller, Chaos **7**, 455 (1997).

[54] S. Tang and J. M. Liu, IEEE J. Quantum Electron. **37**, 329 (2001).

[55] F. Y. Lin and J. M. Liu, Appl. Phys. Lett. **81**, 3128 (2002).

[56] S. C. Chan, IEEE J. Quantum Electron. **46**, 421 (2010).

[57] T. B. Simpson, J. M. Liu, and A. Gavrielides, IEEE J. Quantum Electron. **32**, 1456 (1996).

[58] T. B. Simpson, J. M. Liu, A. Gavrielides, V. Kovanis, and P. M. Alsing, Phys. Rev. A **51**, 4181 (1995).

[59] J. M. Liu, *Photonic Devices* (Cambridge University Press, Cambridge, 2005).

[60] J. M. Liu and T. B. Simpson, IEEE J. Quantum Electron. **30**, 957 (1994).

[61] J. Mulet, C. Masoller, and C. R. Mirasso, Phys. Rev. A **65**, 063815 (2002).

[62] J. P. Zhuang and S. C. Chan, Opt. Express **23**, 2777 (2015).
[63] J. Helms and K. Petermann, IEEE J. Quantum Electron. **26**, 833 (1990).
[64] S. S. Li, X. Zou, L. Wang, A. Wang, W. Pan, and L. Yan, Opt. Express **28**, 21286 (2020).
[65] B. Garbin, J. Javaloyes, G. Tissoni, and S. Barland, Nat. Commun. **6**, 5915 (2015).
[66] J. Javaloyes, T. Ackemann, and A. Hurtado, Phys. Rev. Lett. **115**, 203901 (2015).
[67] L. Larger, B. Penkovsky, and Y. Maistrenko, Nat. Commun. **6**, 7752 (2015).
[68] J. D. Hart, L. Larger, T. E. Murphy, and R. Roy, Philos. Trans. R. Soc. A **377**, 20180123 (2019).
[69] M. Marconi, J. Javaloyes, P. Camelin, D. C. Gonzalez, S. Balle, and M. Giudici, IEEE J. Sel. Top. Quantum Electron. **21**, 1101210 (2015).
[70] A. G. Vladimirov, D. Turaev, and G. Kozyreff, Opt. Lett. **29**, 1221 (2004).
[71] C. Masoller, D. Sukow, A. Gavrielides, and M. Sciamanna, Phys. Rev. A **84**, 023838 (2011).
[72] D. W. Sukow, T. Gilfillan, B. Pope, M. S. Torre, A. Gavrielides, and C. Masoller, Phys. Rev. A **86**, 033818 (2012).